An efficient green protocol for photo-degradation of bromophenol blue dye

Nesrine M.R. Mahmoud[a,*], Hemmat A. Elbadawy[b], Heba M. Refaat[b]

[a]*Department of Basic Sciences, Deanship of Preparatory Year and Supporting Studies, Imam Abdulrahman Bin Faisal University (IAU), Dammam, P.O. Box: 1982, Saudi Arabia (KSA), email: nmmahmoud@iau.edu.sa*
[b]*Chemistry Department, Faculty of Science, Alexandria University, Ibrahimia P.O. Box: 426, Alexandria 21321, Egypt, emails: elbadawy_hm@yahoo.com (H.A. Elbadawy), hebarefaat212@yahoo.com (H.M. Refaat)*

ABSTRACT

Green synthesis is a simple, healthy, ecofriendly approach that has captivated the scientific community's focus worldwide. Recoverable biogenic hematite photocatalyst was fabricated via a one-step green method from a natural bio-waste precursor, namely *Psidium guajava* leaves. The synthesized product was given the name G-Fe$_2$O$_3$-NP's. It was monitored and fully characterized by various analytical techniques, and its photocatalytic activity has been studied for the degradation of aqueous bromophenol blue dye. The pure rhombohedral hematite phase of α-Fe$_2$O$_3$ with needle-like shape crystals of an average size ~(40–50) nm was confirmed via scanning electron microscopy and transmission electron microscopy. Brunauer–Emmett–Teller (BET) analysis displayed that BET surface area and mean pore diameter of the as-synthesized iron oxide nanoparticles were 15.8 m^2 g^{-1} and 14.9 nm, respectively. Results revealed complete degradation of the non-biodegradable dye in 12 min. Furthermore, 97% mineralization was confirmed by TOC removal. Reusability study for the photocatalyst was conducted for five successive cycles and indicated high efficiency of the synthesized hematite in visible light. Additionally, G-Fe$_2$O$_3$-NP's were examined for their antibacterial and antioxidant activities. It showed activity towards both *Pseudomonas aureginosa*, *Staphylococcus aureus*, and mild antioxidant activity.

Keywords: Biocatalyst; Biogenic iron oxide; Bromophenol blue dye; Green synthesis; Degradation

1. Introduction

Urbanization is increasing rapidly around the world, raising demands on natural resources. One of these resources is water which is highly impacted by the negative consequences of urbanization. People suffer from either shortage of freshwater supplies or even declining water quality due to the pollution index increase [1].

Organic pollutants originating from domestic sewage, urban run-off, and industrial effluents are among the more significant wastewater pollutants. Organic dyes, pigments, and coloring agents introduce common contaminants, generating toxic materials into water [2,3]. Bromophenol blue (BPB) is a model example of the triphenylmethane family used in textile dyeing [4]. The pretreatment of the industrial effluents is necessary, especially if they carry a high concentration of this dye due to their toxic impacts on the receiving waters [2]. Biodegradation of organic pollutants into simple green products as carbon dioxide and water is cheap and efficient. Unfortunately, complex organic dyes containing aromatic rings as bromophenols are highly resistible to biodegradation or even decompose naturally very slowly, so that a heavy burden may be caused to the aquatic environment [2]. Other efficient techniques are required as photocatalysis, adsorption, advanced, and electrochemical oxidation systems [5]. Despite these techniques' effectiveness, they might present disadvantages, as introducing pollutants to the treated water, losing valuable catalysts, long term degradation consuming both time and energy.

* Corresponding author.

The reuse of bio-wastes drew attention worldwide due to the challenges of accumulating waste and their disposal costs. Utilizing green chemistry to synthesize non-hazardous, efficient, and reproducible photocatalysts is growing to improve environmental performance. New eco-friendly synthetic strategies emerged to prepare these nanocatalysts via routes that use benign reagents (plant extracts) rather than using the traditional unsafe chemicals (sodium hydroxide and ammonia) [6]. Notable microorganisms, fungi, vitamins B_1, B_2, C, green tea, and other plant extracts [7] in green synthesis. Bio-based nanoparticle size and surface stability are affected by the plant extract source, which may function both as reducing and capping agents [8].

Biogenic synthesis extended to prepare a wide range of metal oxide nanoparticles with interesting and miscellaneous properties [9]. Iron oxide nanoparticles turn up to be one of the promising nanoparticles with advanced surface properties. Multifunctional iron oxide nanoparticles have emerged and are extensively applied in various fields such as catalysis, biomedicine, cosmetics, and materials engineering [10]. Ideal properties of iron oxide nanoparticles such as higher surface area and small energy band gap can also be assigned to a wide range of applications. Among them, nanocrystalline α-Fe_2O_3 which is characterized by a narrow bandgap (2.0–2.2 eV) [11], so accordingly, it is one of the most prominent materials utilized in photocatalytic applications. Besides, α-Fe_2O_3 nanoparticles show good magnetic properties and excellent stability in aqueous solutions [12]. Photocatalytic nanoparticle-based degradation under visible light irradiation is a highly efficient treatment protocol, as it is highly economical and avoids secondary pollution [13,14]. Using biogenic inorganic nanoparticles as antibacterial agents are emerging recently over the use of traditionally organic ones. Different forms of inorganic nanomaterials like powders can be used successfully in neutralizing different varieties of bacteria, either gram-negative or gram-positive bacteria [15]. They are also characterized by higher stability at high temperatures and pressures retaining their medicinal property [16]. Hematite nanocrystals are considered one of the promising inorganic antibacterial agents [17,18].

Establishing ecofriendly nanoparticle-based photocatalyst, which is viable for the destruction of the organic dyes under visible light irradiation, becomes an urgent demand to ensure no transfer of secondary pollutants to the water supplies [9]. Here in this paper, we succeeded in synthesizing the biofunctionalized hematite nanoparticles by an easy one-pot green procedure. Additionally, we applied these nanoparticles to degrade and exclude the photostable, non-biodegradable dye (BPB) from the wastewater. A secondary pollution-free technique was designed to meet environmental challenges by using clean, pure energy from the sun, which is considered very cheap and convenient. Furthermore, G-Fe_2O_3-NP's were examined for their antibacterial and antioxidant activities.

2. Materials and methods

2.1. Materials

BPB ($C_{19}H_{10}Br_4O_5S$) has molecular weight = 669.99 g mol^{-1} and purity > 98% was purchased from Sigma-Aldrich chemical company (St. Louis, MO, USA). Other chemicals used are analytical grade. $FeCl_3 \cdot 6H_2O$ was purchased from S.d.fine-Chem Ltd., India, while H_2O_2 was purchased from Scharlab S.L. Spain. All chemicals are used without further purification.

2.2. Plant "Psidium guajava" extracts preparation

Green synthesis of G-Fe_2O_3-NP's from *Psidium guajava* leaves has been investigated. The first step was to wash the plant leaves with tap water, followed by applying bidistilled water for sterilization. Secondly, the washed plant leaves are kept for 24 h at room temperature to dry and followed by grinding it using a mortar and pestle. A mass of 40 g of the dried plant parts is mixed with 1 L of double distilled water and kept to boil for 30 min. To prepare a clear extract, the mixture is filtered several times using Whatman Grade 1 filter paper. The filtrate obtained is used as a plant extract and is kept in a fridge at 4.0°C.

2.3. Bio-synthesis of G-Fe_2O_3-NP's

A volume of 100 mL of *P. guajava* extract previously prepared was added dropwise into an equal volume of 1.0 M aqueous solution of $FeCl_3$ under continuous stirring of 400 rpm at 80°C. A few hours later, the brownish-yellow color turns gradually to the deep brown color solution and then changed slowly to dark brown precipitate [19]. The prepared precipitate was decanted from the solution, then washed successively by deionized water [9], and dried in the oven overnight at 80°C [10]. The synthesis and reduction process was monitored by UV spectrometry in different time intervals, and the absorption peaks were observed, as illustrated later. The suggested mechanism for forming the G-Fe_2O_3-NP's in the presence of the hydroxyl group of *P. guajava* leaf extract as a capping agent is demonstrated in Fig. 1.

2.4. Characterization

2.4.1. Structural assessment

Fourier transform infrared (FTIR) spectrophotometer (Shimadzu) was used to investigate the functional groups and peculiar spectra of the synthesized G-Fe_2O_3-NP's. The dried extract powder and the synthesized nanoparticles were compressed separately with KBr and tested in parallel [20]. The FTIR spectra of G-Fe_2O_3-NP's and raw guava were determined in the range of 400–4,000 cm^{-1}.

Determination of BPB was carried out by measuring the absorbance of the BPB samples at λ_{max} = 591 nm using a UV-vis double PC 8 auto cell scanning spectrophotometer UV-VIS double beam (Model UVD-3000) [2].

Thermo-gravimetric analysis (TGA-DTA7300, Exstar) was used to test the heat stability of nanoparticles biosynthesized. The test was carried out at room temperature in the range of 25°C–600°C in atmospheric air at a heating rate of 10°C/min in an alumina crucible. Shimadzu XRD X-ray powder diffract meter with Cu Kα radiation (λ = 1.5418 Å) at a scanning speed of 0.2 S was used to recognize the specific peaks of the synthesized G-Fe_2O_3-NP's.

Also, a UV-vis spectrophotometer (Shimadzu Scientific Instruments Incorporated, Maryland, USA) was used at a resolution of 64 nm. Solid disc prepared to detect bonding energy gap of G-Fe_2O_3-NP's [21].
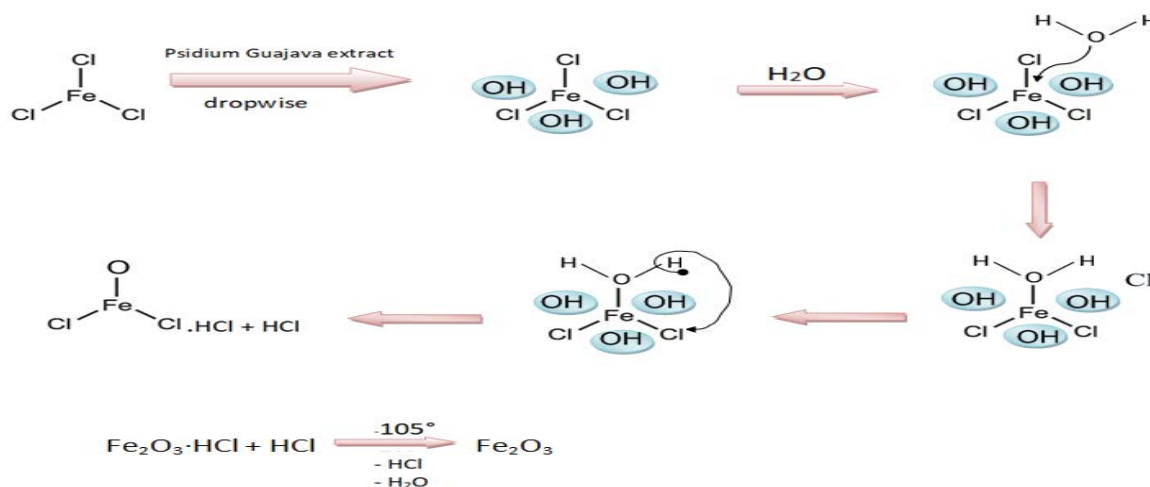
Fig. 1. Suggested mechanism for the formation of the G-Fe$_2$O$_3$-NP's in the presence of hydroxyl group of *Psidium guajava* leaf extract as a capping agent.

Zeta potential was measured using Zetasizer (Malvern Instruments, UK) at 633 nm and a 173° backscattering angle at a fixed refractive index of the respective formulations to assess the stability of metal oxides nanoparticles [21].

2.4.2. Morphological characterizations

Scanning electron microscopy (SEM; FEI, ISPECT S50, Czech Republic) was used to evaluate the morphology and arrangement of the synthesized G-Fe$_2$O$_3$-NP's. SEM was operated at an accelerating voltage of 20 kV and a working distance of about 10 mm. A transmission electron microscopy (TEM), FEI, Morgagni 268, Czech Republic at 80 kV was used to record the specimens' images. Finally, the energy-dispersive X-ray spectroscopy (EDAX) analyses were performed using EDX-8000, Shimadzu [22,23].

2.5. Photocatalytic degradation of BPB dye by G-Fe$_2$O$_3$-NP's

A preliminary study was conducted in the dark condition to measure the extent of the dye's adsorption onto the catalyst's surface. For this purpose, G-Fe$_2$O$_3$-NP's (0.05 g) was shaken with 50 mL of BPB solution (5 × 10^{-4} M) in a stoppered flask in regular intervals of time and then centrifuged [9]. The absorbance of the dye before and after the adsorption process was measured at their λ_{max} (591 nm) to be used for the determination of their removal during the adsorption process. The results showed that the adsorption extent became constant after 30 min contact time. Hence, to eliminate the surface adsorption effect in removing the dye and before the photocatalytic experiment, the dye was shaken with the catalyst for 30 min before irradiation experiments [24]. The biosynthesized nanoparticles' photocatalytic activity has been investigated using an aqueous BPB dye solution as a model pollutant. The mixture was then irradiated under visible light (low-pressure Hg vapor lamp, emitting predominantly at 254 nm and 15 W) for different intervals of time ranging from 0 to 1 h without any pH adjustment (pH = 6.3). After a definite irradiation time, iron oxide nanoparticles were separated by

centrifugation, the absorbance and concentration of BPB solution were determined using a double beam UV-visible spectrophotometer (Model UVD-3000). The samples were regularly removed to determine BPB, both during the dark adsorption stage and photocatalytic degradation. The percent degradation of BPB was calculated with the following equations [25,26]:

$$\% \text{ degradation} = \frac{A_0 - A}{A_0} \times 100 \tag{1}$$

$$\% \text{ degradation} = \frac{C_0 - C}{C_0} \times 100 \tag{2}$$

where A_0 and A represent the absorbance of BPB solution before and after visible light irradiation, respectively. Similarly, C_0 and C are defined as the concentration (mg/L) of BPB solution before and after visible light irradiation, respectively. The λ_{max} of the BPB solution was recorded to be 591 nm. The nano iron oxide catalyst was recycled and reused for five consecutive batches using the above-mentioned conditions [24,25]. In the present study, a solar photocatalytic treatment was implemented at the chemistry department, Alexandria University campus.

2.6. Free radical scavenging activity on DPPH

The antioxidant activity of the G-Fe$_2$O$_3$-NP's was carried out at the Regional Center for Mycology and Biotechnology (RCMB) at Al-Azhar University. The method applied was the already established protocols utilizing the spectrophotometer [27]. Immediate absorbance measurements were reported using a UV-visible spectrophotometer (Milton Roy, Spectronic 1201). The decline in absorbance at 515 nm was recorded continuously at 1 min intervals for 16 min until stable absorbance was reached. Ascorbic acid was used as a positive control. The percentage inhibition (PI) of the DPPH radical was calculated according to the formula:

$$PI = \frac{\left(A_C - A_T\right)}{A_C} \times 100 \qquad (3)$$

where A_C is the absorbance of the control at t = 0 min and A_T is the absorbance of the sample + DPPH at t = 16 min [27]. The dose-response curve's graphic plots were used to estimate 50% inhibitory concentration (IC_{50}), the concentration required to inhibit DPPH radical by 50%.

3. Results and discussion

3.1. Structural characterization

The X-ray diffraction (XRD) spectrum of the G-Fe$_2$O$_3$-NP's, as in Fig. 2, revealed the successful synthesis of the iron oxide nanoparticles. The Bragg peaks were found to be consistent with the single and pure rhombohedral hematite phase of α-Fe$_2$O$_3$ (JCP pattern: 00-003-0800) [28]. The XRD pattern shows various diffraction peaks in the range (20 < 2θ < 80) recorded at 2θ = 24.3°, 33.2°, 35.7°, 40.9°, 49.4°, 54.1°, 57.5°, 62.4°, 64°, and 71.7° corresponding to crystallographic reflections of 012, 104, 110, 113, 024, 116, 214, 300, and 010 were elucidated. XRD patterns showed confined sharp narrow peaks, which indicate high purity and crystallinity of the synthesized hematite particles [29]. The high purity could recommend the catalytic activity for G-Fe$_2$O$_3$-NP's [30].

The complex nature of the samples biosynthesized could be observed from the FTIR spectra, which showed several absorption peaks (Fig. 3). The raw guava showed a robust broadband in the range 3,410–3,426 cm^{-1} assigned to an N–H as well as an O–H stretching vibration attributed to intramolecular and intermolecular hydrogen bonding of polymeric compounds, indicating the presence of "free" hydroxyl alcoholic and phenolic groups [31]. A sharp peak at 2,910 cm^{-1} indicating the presence of aromatic ring (Ar–H) and glucose moieties (CH$_2$OH) in tannins which was shifted to 2,900 cm^{-1} in modified iron oxide capped with extract moieties. An absorption band at 2,368 cm^{-1} was observed with low intensity in raw guava and with higher intensity in G-Fe$_2$O$_3$-NP's attributed to the symmetric stretching vibration of CH$_2$ due to C–H bonds of aliphatic acids [32]. The sharp
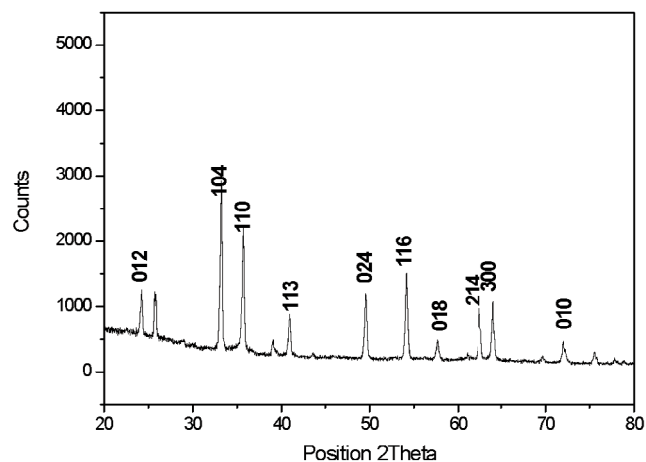
peaks around 1,629 and 1,610 cm^{-1} were attributed to the C=C stretching vibration in the phenolic groups for raw guava and G-Fe$_2$O$_3$-NP's, respectively [33].

The bands at 1,027 and 1,123 cm^{-1}, respectively, were due to the C–O stretching attributed to biological moieties for raw guava leaves and bio-modified iron oxide nanoparticles. 709–864 cm^{-1} assigned to O–H out of plane blending, which disappeared in the case of G-Fe$_2$O$_3$-NP's due to interaction with aqueous iron(III) chloride to form iron(III) hydroxide. The strong absorption band can confirm the presence of G-Fe$_2$O$_3$-NP'sd at 555 and 490 cm^{-1} [34]. These two bands developed from the split of the υ_1 band at 555 cm^{-1}, which is attributed to the Fe–O bond on the Iron oxide NPs surface and biological moiety interfaces.

In comparison with the iron(III) chloride aqueous solution used in the preparation, the UV-vis spectrum of iron oxide nanoparticles is displayed in Fig. 4. A phenotypic change in the yellow color of FeCl$_3$ is observed by the absorption spectra data of G-Fe$_2$O$_3$-NP's, which revealed a sharp absorption peak at 407 nm, missing in FeCl$_3$, and can indicate iron oxide formation [35].

Thermal analysis (TGA, differential gravimetric analysis (DTA)) for the pure biogenic hematite synthesized from guava leaves extract is illustrated in Fig. 5. The percent of weight loss at different temperature decomposition ranges, T_{max}, T_{10}, and % residue, are expressed in Table 1 [36,37]. It can be observed that thermal decomposition of the biosynthesized oxide takes place via two stages. The first decomposition step proceeded from 53°C to 156°C while the second step range was between 156°C and 319°C. The first small mass loss (4%) corresponds to the superficial water.
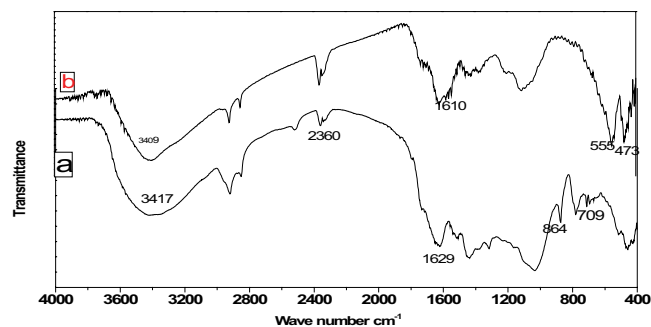

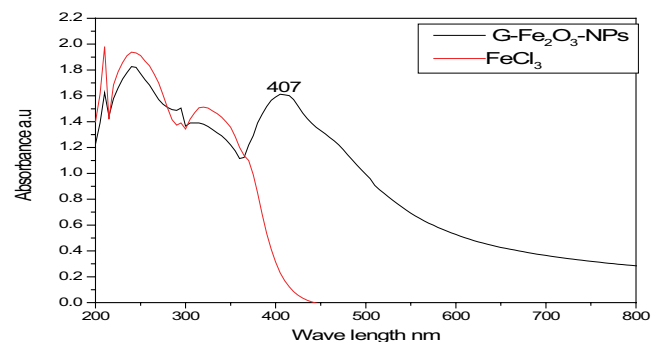
Fig. 3. FTIR spectra of: (a) raw guava leaves and (b) G-Fe$_2$O$_3$-NP's.

Fig. 2. XRD spectrum of G-Fe$_2$O$_3$-NP's.

Fig. 4. UV-vis spectra of Fe(III) chloride and G-Fe$_2$O$_3$-NP's.

The DTA shows a corresponding endothermic peak in the same temperature range (Fig. 5b). In contrast, the second loss (11%) may be assigned to the capping agent residual as it is associated with removing organic compound skeletons that were interrupted and broken down. This loss in weight (11%) is confirmed in DTA exothermic sharp peak in the 180°C–400°C temperature range. It can be concluded from TGA that above 400°C, there is no observable loss of mass, which recommends that the temperature above 400°C is the suitable calcination temperature under air atmosphere, consistent with the results previously reported [38].

3.2. Morphological characterization

The morphological specifications of a catalyst are essential since they affect its catalytic performance [39,40]. Investigation of the biogenic G-Fe$_2$O$_3$-NP's morphology was studied through high-resolution SEM and TEM as indicated in Figs. 6a and b. Needle-like crystals of an average size of ~(40–50) nm were aggregated on the surface, giving the appearance of rhombohedral structures consistent with XRD Fig. 2 and confirmed by the TEM images. Particle size distribution was studied through TEM images via digitalization using j-image software (Fig. 6d). The EDX spectroscopy was performed to know the surface composition and distribution of elements for the stabilized iron oxide nanoparticles reduced using the guava leaf extract is shown in Fig. 6c. The EDX spectrum was mainly constituted with iron peaks around 6.1 and 7.2 keV, which confirms biosynthesized iron nanoparticles' formation.

The bandgap of G-Fe$_2$O$_3$-NPs samples was calculated using the mathematical formula $E = hc/\lambda$, where c the velocity of light, h is the Plank's constant, and λ the wavelength [41]. The energy bandgap of the green synthesized hematite nanoparticles was found to be 2.43 eV. The observed value aligns with the reported values in the range 1.95 to 2.35 eV [42,43]. The slight difference in the calculated value may be attributed to the size of the nanoparticles. As band gap widening of nanomaterials is assigned to the quantum mechanical effects of the low-dimensional crystallites [44]. The value recorded enabled us to apply the as prepared iron oxide nanoparticles as a photocatalyst in the presence of visible light because they could collect up to 40% of the solar spectrum energy [11,45].

Barrett–Joyner–Halenda (BJH) analyses are employed for pore area and specific pore volume determination, using adsorption and desorption techniques. The nitrogen adsorption–desorption isotherms and the BJH desorption pore size distributions of raw guava and the G-Fe$_2$O$_3$-NP's, shown in the Supplementary File, and the data are presented in Table 2. The adsorption–desorption isotherms are type IV with H$_3$-type, revealing that both materials are mainly mesoporous, characterized by a hysteresis loop, accompanied by capillary condensation mesoporous, and the limiting uptake over a range of high p/p^0 [46]. The adsorbed volume is sharply increased at a relative pressure (P/P^0) of approximately, representing capillary condensation of N$_2$ in the homogeneous mesopores. The inflection position shows a slight shift toward lower relative pressures and an increase in the quantity of adsorbed nitrogen in G-Fe$_2$O$_3$-NPs relative to raw guava attributed to the destruction of the guava raw framework and the pore diameter increase via complex formation with Fe$_2$O$_3$-NPs. It worth mentioning that the Brunauer–Emmett–Teller-surface area (BET) of 5.5550 m^2/g and BJH desorption volume of 2.1142 × 10^{-2} cm^3/g were obtained for raw guava leaves and increased to 15.765 m^2/g and 5.9375 × 10^{-2} cm^3/g, respectively, for G-Fe$_2$O$_3$-NPs. Besides, the mean pore diameter of the guava raw 14.352 nm was increased to 14.898 nm. The increase in surface area, pore diameter, and pore volume were probably due to the loss of volatile organic compounds, which eventually increase the materials' porosity [40]. However, the pore diameter lies in the range reported for the mesoporous structure [47]. Generally, the variation of BET surface area, BJH desorption cumulative volume, and pore diameter of pores point out the variety in the morphology and crystallinity because of complex formation. The positive value of adsorption constant, C, 3.390, 19.371 for guava-raw and G-Fe$_2$O$_3$-NPs, respectively, indicates the exothermic nature of the adsorption process, with higher N$_2$ affinity of G-Fe$_2$O$_3$-NPs ($C = e^{(\Delta H_1 - \Delta H_L)/RT}$, ΔH_1 is the heat of N$_2$ adsorption of monolayer cross-section area, ΔH_L is the net heat of N$_2$ adsorption, R and T are the gas constant and absolute temperature, respectively). It worth mentioning that the surface area of G-Fe$_2$O$_3$-NPs, is about three times higher
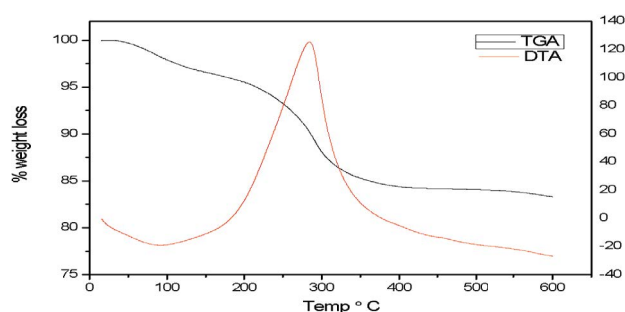

Fig. 5. (a) TGA and (b) DTA of G-Fe$_2$O$_3$-NP's.

Table 1
TGA data of biogenic G-Fe$_2$O$_3$-NP's

Sample name	% Weight loss at various temperature (°C)						Decomposition temperature range (°C)		T_{max} [a] (°C)		T_{10} [b] (°C)	% residue
	100°C	200°C	300°C	400°C	500°C	600°C	Step I	Step II	Step I	Step II		
G-Fe$_2$O$_3$-NP's	2.4	4.6	12.1	15.6	16.0	16.5	53–156	156–391	86	286	284	83.5

*[a]T_{max}: Temperature for maximum rate of decomposition and [b]T_{10}: Temperature for 10% weight loss.
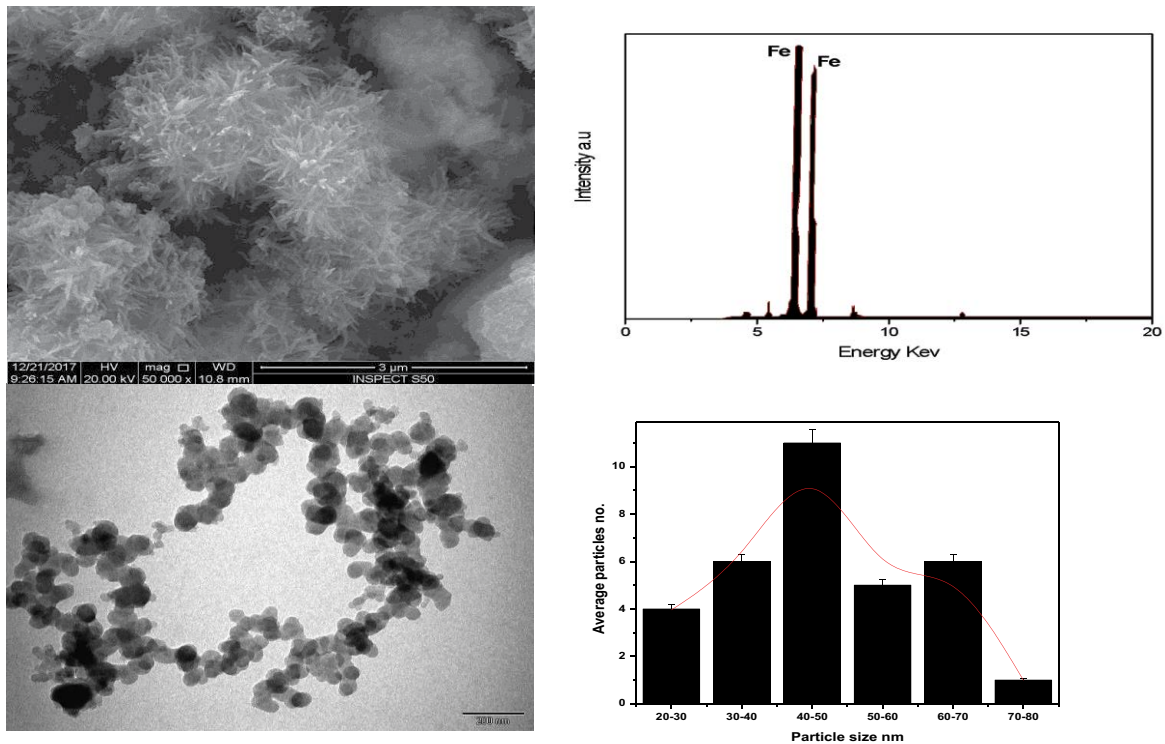
Fig. 6. (a) SEM, (b) TEM, (c) EDX, and (d) particle size distribution of G-Fe$_2$O$_3$-NP's.

Table 2
Porosity studies of guava raw and as prepared sample, G-Fe$_2$O$_3$-NP's

Property	Guava leaves-raw	G-Fe$_2$O$_3$-NP's
BET surface area (m^2/g)	5.5550	15.7651
BJH desorption cumulative volume (cm^3/g)	2.1142×10^{-2}	5.9375×10^{-2}
BJH desorption average pore diameter (nm)	14.352	14.898
Adsorption constant	3.3900	19.871

than the commercial α-Fe$_2$O$_3$ (6.0 m^2/g), which indicates its potential activity for hydroxyl radical formation and hence its higher photocatalytic degrading effect [48,49].

3.3. Photocatalytic activity

Fig. 7 shows the course of degradation of 5'10^{-4} M BPB dye, which was measured in terms of its absorbance in equal intervals of time in the following conditions: (i) under visible light irradiation in the absence of the photocatalyst, (ii) in the presence of the 1 g/L catalyst G-Fe$_2$O$_3$-NPs only, (iii) in the presence of 0.002 mM H$_2$O$_2$ only and finally, and (iv) in the presence of both catalyst 1 g/L G-Fe$_2$O$_3$-NPs and 0.002 mM H$_2$O$_2$. It is obvious in Fig. 7a that the BPB has high photostability [2], that is, there was no significant photo-degradation by direct photolysis. Only 3.0% of the dye was degraded during the whole time of the experiment, while complete photodegradation of the BPB dye was observed in G-Fe$_2$O$_3$-NPs and under visible light irradiation, which was achieved efficiently during a short time interval lasts 12 min only (Fig. S1). This was followed by the decrease in absorbance with time, signifying the decrease in residual dye concentration in solution, and signifying dye degradation.

Boosting the dye's degradation rate in the photocatalyst's presence was monitored by changing the color intensity of the dye and measuring the percentage of total organic carbon removal (TOC). Decolorization and almost complete mineralization were maintained through an irradiation time (12 min) and was confirmed by the TOC removal rate, as a sharp decrease is recoded, reaching nearly less than 3.0% after degradation.

The reaction kinetics showed that the reaction followed pseudo-first-order kinetics confirmed from the plot of ln(C_0/C) vs. irradiation time of the degradation process of BPB, which follows a linear relationship with rate constant equals 0.231 min^{-1} [9], which was determined from the slope of the linear fitting line as shown in Fig. 7b. As it can be observed, a good correlation to the pseudo-first-order reaction kinetics ($r^2 > 0.97$) was found. The observed super efficiency of G-Fe$_2$O$_3$-NPs for complete mineralization of organic dyes may be explained in terms of the stable complex between BPB* and Fe^{+3}, which can absorb visible
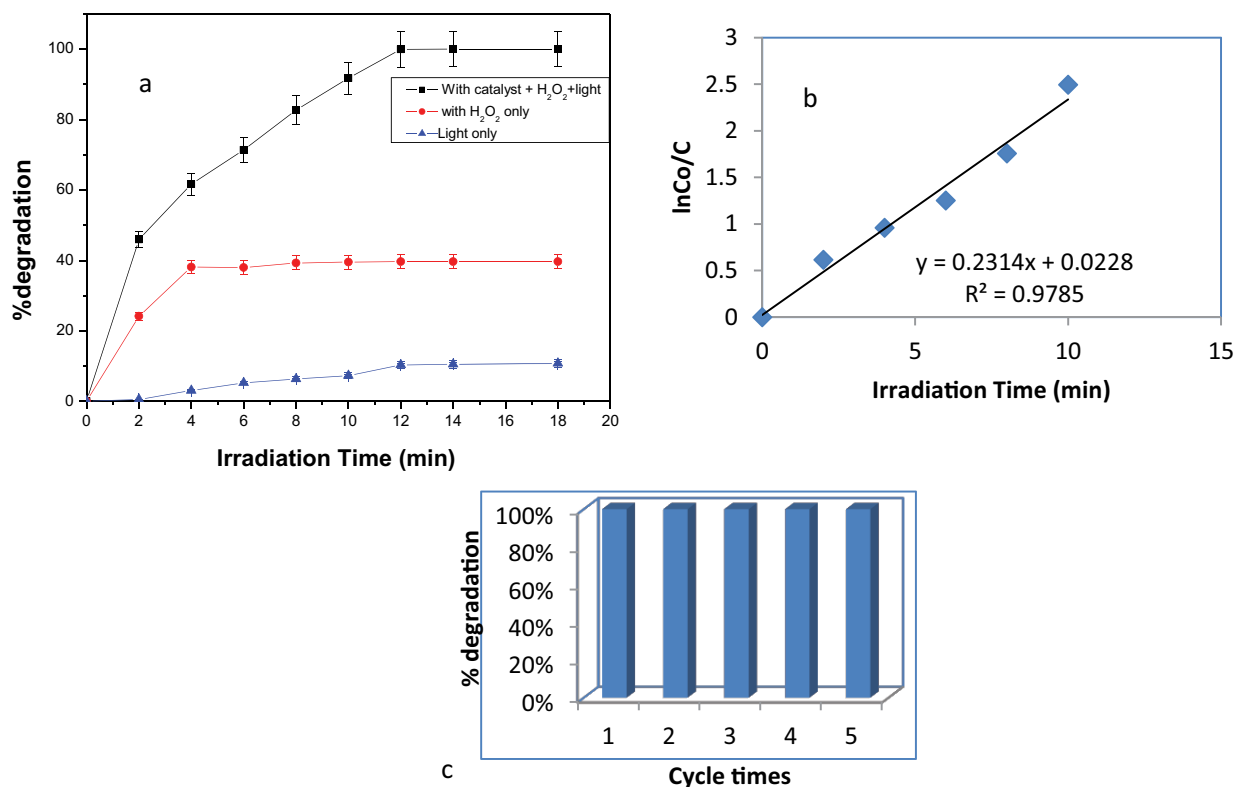
Fig. 7. Photocatalytic activity: (a) solar degradation, (b) kinetics, and (c) reuse.

light and successfully produces BPB*+ and Fe+3 [50], which is reduced later into Fe+2 via inter-molecular electron transfer from an excited dye state [51]. Other primary key factors in heterogeneous catalysis are the catalyst particle size (40–50 nm), and BET S.A, which are assumed to enhance the biosynthesized photocatalyst's performance. A study for solar photocatalytic treatment was carried out to investigate the applicability of using natural sunlight as a visible light source. This trial results showed high consistency with the results obtained using the Hg lamp, which is a key indicator of utilizing solar light in the degradation process as it is available, cost-effective, and energy-saving [52].

The green synthesized hematite catalyst was successfully recycled and reused for five consecutive trials. The hematite nanoparticles were washed and dried after each degradation experiment to be reused in the following cycle. The results showed no recorded decrease in the nanocatalyst's photocatalytic activity, maintaining the same efficiency during the five cycles investigated, as shown in Fig. 7c. This feature recommends high stability of the as-prepared photocatalyst that would further expand its usage in the remediation of wastewater. In literature, some catalysts' photocatalytic properties declined after successive batches during the reusability test [24].

3.4. Biological activity

3.4.1. Antioxidant activity

The DPPH assay [53] determined the antioxidant potential of G-Fe$_2$O$_3$-NP's. It was recorded that the

inhibition percentage of free radicals is affected by the concentration of the sample (Table S1). The synthesized sample showed antioxidant activity with IC$_{50}$ = 579.9 μg/mL relative to IC$_{50}$ = 14.2 μg/mL recorded for the reference compound ascorbic acid [54]. The lower antioxidant activity recorded for G-Fe$_2$O$_3$-NP's may be attributed to the lower radical-scavenging activity of guava leaves extract in water. So, it is recommended to use ethanol extract due to its higher phenolic content, enhancing their antioxidant activity, as suggested in previous studies [53,55].

3.4.2. Antibacterial activity

The antibacterial activity of the biogenic nanoparticles was screened against both gram-negative and gram-positive species. A significant growth inhibition zone was observed in *Staphylococcus aureus* and *Pseudomonas aerugino*sa with 12 and 13 mm diameter, respectively. The antibacterial nature of the iron oxide NP's has been well-established [56]. Based on these preliminary results, it can be concluded that G-Fe$_2$O$_3$-NP's could be further explored and used in future studies in antimicrobial activity.

4. Conclusions

Biogenic iron oxide nanoparticles(G-Fe$_2$O$_3$-NP's) were successfully synthesized via a fast, cost-effective, and biosafe green route. G-Fe$_2$O$_3$-NP's were fully characterized to elucidate both stability and functionality of G-Fe$_2$O$_3$-NP's. The XRD revealed that the photocatalyst was composed of rhombohedral Fe$_2$O$_3$. SEM analysis showed needle-like

nanoparticle morphology. BET surface area of the as-prepared nanoparticles is about 3 times higher than that of the commercial α-Fe$_2$O$_3$ nanoparticles. An energy band gap of 2.43 was calculated, which elucidates the catalyst's ability to collect visible light during the degradation process. The high performance of the as-synthesized G-Fe$_2$O$_3$-NP's as a photocatalyst was evaluated via complete mineralization of BPB dye within 12 min under visible light irradiation and with a rate constant estimated to be 0.231 min^{-1}. Besides, the biological activity of the nanoparticles was screened as a preliminary study for our future work. Furthermore, the photocatalyst showed high reusability several times without any significant loss of photocatalytic activity. Finally, these NPs may be applied as a bio-functionalized photocatalyst.

Acknowledgments

References

[1] E. Tetteh, S. Rathilal, Adsorption and photocatalytic mineralization of bromophenol blue dye with TiO$_2$ modified with clinoptilolite/activated carbon, Catalysts, 11 (2020) 1–14, doi: 10.3390/catal11010007.

[2] N. Bouanimba, R. Zouaghi, N. Laid, T. Sehili, Factors influencing the photocatalytic decolorization of Bromophenol blue in aqueous solution with different types of TiO$_2$ as photocatalysts, Desalination, 275 (2011) 224–230.

[3] S. Alkaykh, A. Mbarek, E.E. Ali-Shattle, Photocatalytic degradation of methylene blue dye in aqueous solution by MnTiO$_3$ nanoparticles under sunlight irradiation, Heliyon, 6 (2020) e03663, doi: 10.1016/j.heliyon.2020.e03663.

[4] S. Djepang, S. Laminsi, E. Njoyim-Tamungang, C. Ngnintedem Yonti, J.L. Brisset, Plasma-chemical and photo-catalytic degradation of bromophenol blue, Chem. Mater. Eng., 2 (2014) 14–23.

[5] E.K. Tetteh, S. Rathilal, Application of magnetized nanomaterial for textile effluent remediation using response surface methodology, Mater. Today: Proc., 38 (2021) 700–711.

[6] R. Varma, Nano-catalysts: key to the greener pathways leading to sustainability, J. Thermodyn. Catal., 3 (2012) e105, doi: 10.4172/2157-7544.1000e105.

[7] M.N. Nadagouda, R.S. Varma, A greener synthesis of core (Fe, Cu)-shell (Au, Pt, Pd, and Ag) nanocrystals using aqueous vitamin C, Cryst. Growth Des., 7 (2007) 2582–2587.

[8] S. Machado, S.L. Pinto, J.P. Grosso, H.P.A. Nouws, J.T. Albergaria, C. Delerue-Matos, Green production of zero-valent iron nanoparticles using tree leaf extracts, Sci. Total Environ., 445–446 (2013) 1–8.

[9] I. Ali, N. Hasan, M. Ahmad, Z. Khan, Biosynthesis of iron nanoparticles using *Trigonella foenum-graecum* seed extract for photocatalytic methyl orange dye degradation and antibacterial applications, J. Photochem. Photobiol., B, 183 (2018) 154–163.

[10] A.T. Khalil, M. Ovais, I. Ullah, M. Ali, Z. Khan, Biosynthesis of iron oxide (Fe$_2$O$_3$) nanoparticles via aqueous extracts of *Sageretia thea* (Osbeck) and their pharmacognostic properties, Green Chem. Lett. Rev., 10 (2017) 186–201.

[11] M.A. Sharifah, B. Abdul, Green synthesis of α-Fe$_2$O$_3$ nanoparticles for photocatalytic application, J. Mater. Sci.: Mater. Electron., 25 (2014) 3572–3577.

[12] A. Umar, M.S. Akhtar, G.N. Dar, S. Baskoutas, Low-temperature synthesis of α-Fe$_2$O$_3$ hexagonal nanoparticles for environmental remediation and smart sensor applications, Talanta, 116 (2013) 1060–1066.

[13] R.A. Crane, T.B. Scott, Nanoscale zero-valent iron: future prospects for an emerging water treatment technology, J. Hazard. Mater., 211–212 (2012) 112–125.

[14] F. Gandomi, S.M. Peymani Motlagh, M. Rostami, A. Sobhani-Nasab, M. Fasihi-Ramandi, M. Eghbali-Arani, R. Ahmadian, N. Gholipour, M. Rahimi-Nasrabadi, M. Ganjali, Simple synthesis and characterization of Li$_{0.5}$Fe$_{2.5}$O$_4$, LiMg$_{0.5}$Fe$_2$O$_4$ and LiNi$_{0.5}$Fe$_2$O$_4$, and investigation of their photocatalytic and anticancer properties on hela cells line, J. Mater. Sci.: Mater. Electron., 30 (2019) 19691–19702, doi: 10.1007/s10854-019-02320-x.

[15] H. Foster, I. Ditta, S. Varghese, A. Steele, Photocatalytic disinfection using titanium dioxide: spectrum and mechanism of antimicrobial activity, Appl. Microbiol. Biotechnol., 90 (2011) 1847–1868.

[16] Y. Xia, Nanomaterials at work in biomedical research, Nat. Mater., 7 (2008) 758–760.

[17] A. Raghunath, E. Perumal, Metal oxide nanoparticles as antimicrobial agents: a promise for the future, Int. J. Antimicrob. Agents, 49 (2017) 137–152.

[18] M. Thukkaram, S. Sitaram, S. Kannaiyan, G. Subbiahdoss, Antibacterial efficacy of iron-oxide nanoparticles against biofilms on different biomaterial surfaces, Int. J. Biomater., 2014 (2014) 1–6.

[19] R.M. Mohamed, D. Mckinney, M.W. Kadi, I.A. Mkhalid, W. Sigmund, Platinum/zinc oxide nanoparticles: enhanced photocatalysts degrade malachite green dye under visible light conditions, Ceram. Int., 42 (2016) 9375–9381.

[20] W.I. Abdel-Fattah, M.M. Eid, S.I. Abd El-Moez, E. Mohamed, G.W. Ali, Synthesis of biogenic Ag@Pd core-shell nanoparticles having anti-cancer/anti-microbial functions, Life Sci., 183 (2017) 28–36.

[21] J.R. Nair, C. Gerbaldi, M. Destro, R. Bongiovanni, N. Penazzi, Reactive & functional polymers methacrylic-based solid polymer electrolyte membranes for lithium-based batteries by a rapid UV-curing process, React. Funct. Polym., 71 (2011) 409–416.

[22] D. Gabr, Significance of fruit and seed coat morphology in taxonomy and identification for some species of Brassicaceae, Am. J. Plant Sci., 09 (2018) 380–402.

[23] H. Mohamed, S. Mohamed, Rutile TiO$_2$ nanorods/MWCNT composites for enhanced simultaneous photocatalytic oxidation of organic dyes and reduction of metal ions, Mater. Res. Express, 5 (2018) 015057, doi: 10.1088/2053-1591/aaa73b.

[24] A. Nezamzadeh-Ejhieh, H. Zabihi-Mobarakeh, Heterogeneous photodecolorization of mixture of methylene blue and bromophenol blue using CuO-nano-clinoptilolite, J. Ind. Eng. Chem., 20 (2014) 1421–1431.

[25] H. Khan, A.K. Khalil, A. Khan, K. Saeed, N. Ali, Photocatalytic degradation of bromophenol blue in aqueous medium using chitosan conjugated magnetic nanoparticles, 33 (2016) 2802–2807.

[26] S. Valizadeh, M.H. Rasoulifard, M. Saeed, S. Dorraji, Adsorption and photocatalytic degradation of organic dyes onto crystalline and amorphous hydroxyapatite: optimization, kinetic and isotherm studies, Korean J. Chem. Eng., 33 (2016) 481–489.

[27] G.C. Yen, P. Der Duh, Scavenging effect of methanolic extracts of peanut hulls on free-radical and active-oxygen species, J. Agric. Food Chem., 42 (1994) 629–632.

[28] J. Su, S. Liu, J. Wang, C. Liu, Y. Li, D. Wu, Solution-based synthesis of carbon–hematite composite thin films for high-performance supercapacitor applications, MRS Commun., 6 (2016) 1–8.

[29] D. Hassan, A.T. Khalil, J. Saleem, A. Diallo, Z.K. Shinwari, M. Maaza, Biosynthesis of pure hematite phase magnetic iron oxide nanoparticles using floral biosynthesis of pure hematite phase magnetic iron oxide nanoparticles using floral extracts of *Callistemon viminalis* (bottlebrush): their physical properties and novel biol, Artif. Cells Nanomed. Biotechnol., 46 (2018) 693–707.

[30] N. Basavegowda, K. Mishra, Y.R. Lee, Synthesis, characterization, and catalytic applications of hematite (α-Fe$_2$O$_3$) nanoparticles as reusable nanocatalyst, Adv. Nat. Sci.: Nanosci. Nanotechnol., 8 (2017) 1–6.

[31] L. Falcão, M.E.M. Araújo, Tannins characterization in historic leathers by complementary analytical techniques ATR-FTIR, UV-vis and chemical tests, J. Cult. Heritage, 14 (2013) 499–508.

[32] O. Abdelwahab, O. Fouad, N.K. Amin, H. Mandor, Kinetic and thermodynamic aspects of cadmium adsorption onto raw and activated guava (*Psidium guajava*) leaves, Environ. Prog. Sustainable Energy, 34 (2015) 351–358.

[33] A. Florido, C. Valderrama, J.A. Arévalo, I. Casas, M. Martínez, N. Miralles, Application of two sites non-equilibrium sorption model for the removal of Cu(II) onto grape stalk wastes in a fixed-bed column, Chem. Eng. J., 156 (2010) 298–304.

[34] S. Bruni, F. Cariati, M. Casu, A. Lai, A. Musinu, G. Piccaluga, S. Solinas, IR and NMR study of nanoparticle-support interactions in a Fe_2O_3-SiO_2 nanocomposite prepared by a sol–gel method, Nanostruct. Mater., 11 (1999) 573–586.

[35] P. Mallick, B.N. Dash, X-ray diffraction and UV-visible characterizations of α-Fe_2O_3 nanoparticles annealed at different temperature, Nanosci. Nanotechnol., 3 (2013) 130–134.

[36] M.I. Shekh, K.P. Patel, R.M. Patel, Electrospun ZnO nanoparticles doped core-sheath nanofibers: characterization and antimicrobial properties, J. Polym. Environ., 26 (2018) 4376–4387.

[37] M.I. Shekh, D.M. Patel, N.N. Patel, U.S. Patel, K.P. Patel, R.M. Patel, Methacrylate copolymers and their composites with nano CdS: synthesis, characterization, thermal behavior, and antimicrobial properties, Int. J. Ind. Chem., 9 (2018) 153–166.

[38] D. Garcia, G. Picasso, P. Hidalgo, H.E.M. Peres, R. Sun Kou, J.M. Gonçalves, Sensors based on Ag-loaded hematite (α-Fe_2O_3) nanoparticles for methyl mercaptan detection at room temperature, Anal. Chem. Res., 12 (2017) 74–81.

[39] N. Hossain, J. Zaini, T.M.I. Mahlia, A.K. Azad, Elemental, morphological and thermal analysis of mixed microalgae species from drain water, Renewable Energy, 131 (2019) 617–624.

[40] N. Hossain, N. Sabzoi, G. Griffin, P. Selvakannan, M. Mujawar, T.M.I. Mahlia, Synthesis and characterization of rice husk biochar via hydrothermal carbonization for wastewater treatment and biofuel production, Sci. Rep., 10 (2020) 1–15.

[41] P. Vanathi, P. Rajiv, R. Sivaraj, Synthesis and characterization of Eichhornia-mediated copper oxide nanoparticles and assessing their antifungal activity against plant pathogens, Bull. Mater. Sci., 39 (2016) 1165–1170.

[42] A.J. Deotale, R.V. Nandedkar, Correlation between particle size, strain and band gap of iron oxide nanoparticles, Mater. Today: Proc., 3 (2016) 2069–2076.

[43] M. Saleem, S.M.A. Durrani, Optical properties of iron oxide (α-Fe_2O_3) thin films deposited by the reactive evaporation of iron, J. Alloys Compd., 521 (2012) 178–182.

[44] N. Kamarulzaman, M.F. Kasim, R. Rusdi, Band gap narrowing and widening of ZnO nanostructures and doped materials, Nanoscale Res. Lett., 10 (2015) 1–12, doi: 10.1186/s11671-015-1034-9.

[45] G. Sharma, A. Kumar, S. Sharma, M. Naushad, P. Dhiman, D.N. Vo, F.J. Stadler, Fe_3O_4/ZnO/Si_3N_4 nanocomposite based photocatalyst for the degradation of dyes from aqueous solution, Mater. Lett., 278 (2020) 1–5, doi: 10.1016/j.matlet.2020.128359.

[46] K. Sing, Reporting physisorption data for gas/solid systems with special reference to the determination of surface area and porosity (Recommendations 1984), Pure Appl. Chem., 57 (1985) 603–619, doi: 10.1351/pac198557040603.

[47] M.I. McGlsham, Internationally recommended names and symbols for physicochemical quantities and units, Annu. Rev. Phys. Chem., 24 (1973) 51–76.

[48] V. Ponnusami, S. Vikram, S.N. Srivastava, Guava (*Psidium guajava*) leaf powder: novel adsorbent for removal of methylene blue from aqueous solutions, J. Hazard. Mater., 152 (2008) 276–286.

[49] B. Ahmmad, K. Leonard, S. Islam, J. Kurawaki, M. Muruganandham, T. Ohkubo, Y. Kuroda, Green synthesis of mesoporous hematite (α-Fe_2O_3) nanoparticles and their photocatalytic activity, Adv. Powder Technol., 24 (2013) 160–167.

[50] M.M. El-Moselhy, Photo-degradation of acid red 44 using Al and Fe modified silicates, J. Hazard. Mater., 169 (2009) 498–508.

[51] A.D. Bokare, W. Choi, Review of iron-free Fenton-like systems for activating H_2O_2 in advanced oxidation processes, J. Hazard. Mater., 275 (2014) 121–135.

[52] P. Dhiman, S. Sharma, A. Kumar, M. Shekh, G. Sharma, Rapid visible and solar photocatalytic Cr(VI) reduction and electrochemical sensing of dopamine using solution combustion synthesized ZnO–Fe_2O_3 nano heterojunctions: mechanism elucidation, Ceram. Int., 46 (2020) 12255–12268.

[53] T. Yamaguchi, H. Takamura, T. Matoba, J. Terao, HPLC method for evaluation of the free radical-scavenging activity of foods by using 1,1-diphenyl-2-picrylhydrazyl, Biosci. Biotechnol., Biochem., 62 (1998) 1201–1204.

[54] S. Bahramikia, R. Yazdanparast, Antioxidant efficacy of *Nasturtium officinale* extracts using various *in vitro* assay systems, J. Acupunct. Meridian Stud., 3 (2010) 283–290.

[55] V. Nihorimbere, Antioxidant power of phytochemicals from *Psidium guajava*, J. Zhejiang Univ. Sci., 5 (2004) 676–683.

[56] R. Irshad, K. Tahir, B. Li, A. Ahmad, A.R. Siddiqui, S. Nazir, Antibacterial activity of biochemically capped iron oxide nanoparticles: a view towards green chemistry, J. Photochem. Photobiol., B, 170 (2017) 241–246.
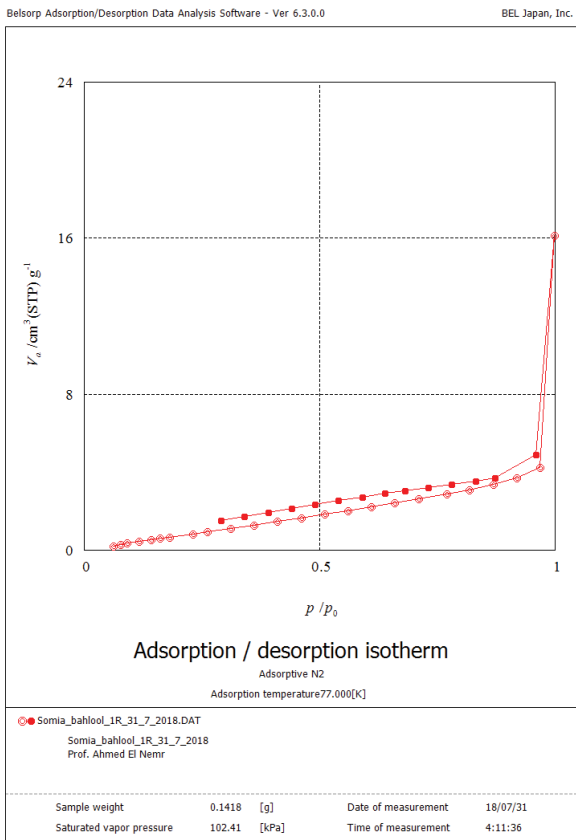
Supplementary information:

Adsorption / desorption isotherm
Adsorptive N2
Adsorption temperature 77.000[K]

Adsorption / desorption isotherm
Adsorptive N2
Adsorption temperature 77.000[K]

Table S1
Antioxidant Activity of G-Fe$_2$O$_3$-NP's using DPPH scavenging

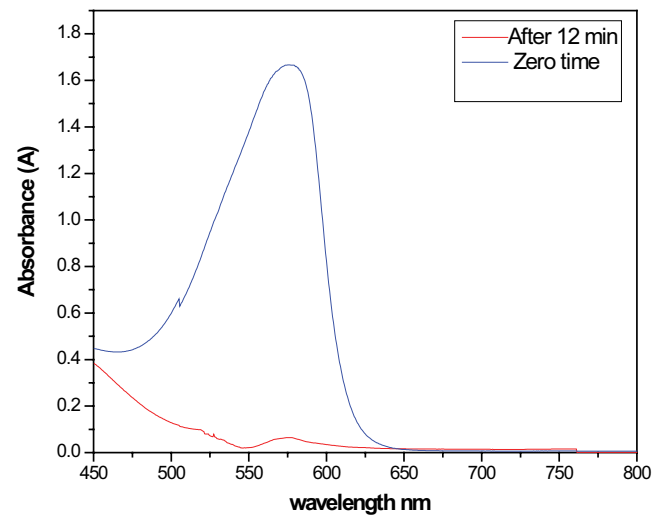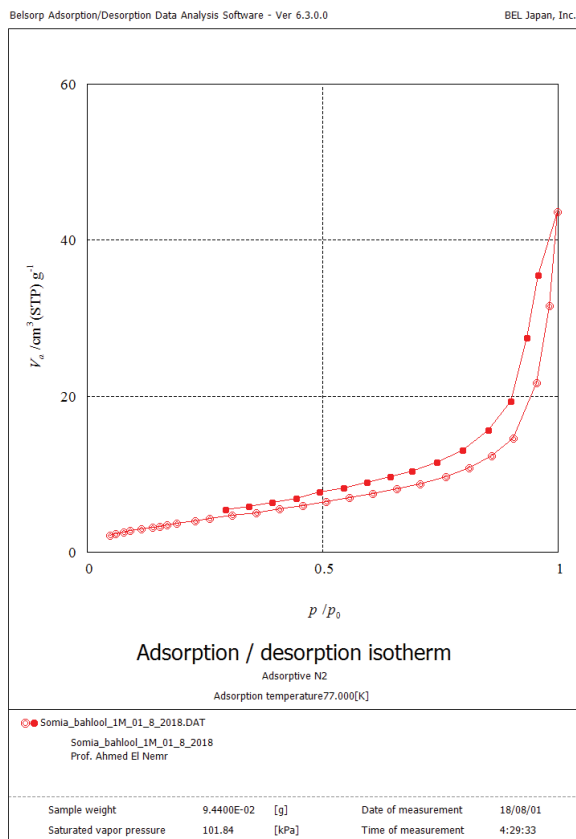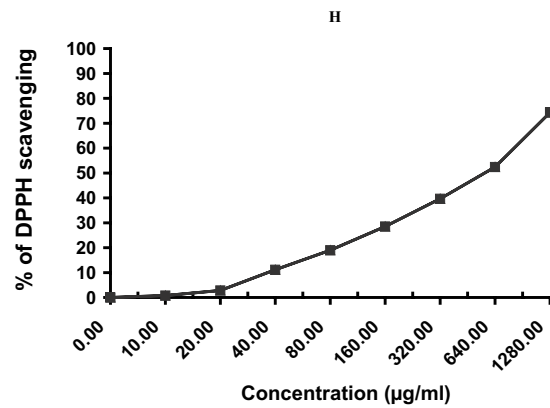| Sample concentration (μg/mL)	DPPH scavenging (%)	Error (±)
1,280	74.32	3.716
640	52.39	2.6195
320	39.66	1.983
160	28.52	1.426
80	18.98	0.949
40	11.14	0.557
20	2.84	0.142
10	0.8	0.04
0	0	0

Fig. S1. Decrease absorption spectra of 50 mL of BPB solution (5 ´ 10^{-4} M) BPB in the presence of G-Fe$_2$O$_3$-NP's (0.05 g) at an irradiation time interval of 12 min; pH = 6.3.